# Optical and electronic properties of transparent conducting Ta:TiO 2 thin and ultra-thin films: the effect of doping and thickness

Beatrice R Bricchi, Maria Sygletou, Luca Ornago, Giancarlo Terraneo, Francesco Bisio, Cristina Mancarella, Lorenzo Stasi, Francesco Rusconi, Erika Mogni, Matteo Ghidelli, et al.

ARTICLE

# Optical and electronic properties of transparent conducting Ta:$TiO_2$ thin and ultra-thin films: effect of doping and thickness

Received 00th January 20xx,
Accepted 00th January 20xx

DOI: 10.1039/x0xx00000x

Beatrice R. Bricchi,*[a] Maria Sygletou,[b] Luca Ornago,[a] Giancarlo Terraneo,[c,d] Francesco Bisio,[e] Cristina Mancarella,[a] Lorenzo Stasi,[a] Francesco Rusconi,[f] Erika Mogni,[f] Matteo Ghidelli,[g] Paolo Biagioni [f] and Andrea Li Bassi[a,d]

The development of low-dimensional transparent conducting systems is nowadays gaining interest in view of novel optoelectronic applications. In this paper, we investigate the evolution of optical and electronic properties of Ta-doped $TiO_2$ films as thickness is decreased down to 5 nm and as a function of Ta doping (5-10% at.), and we correlate the observed behavior to the structural properties, showing a high degree of tunability. Ta:$TiO_2$ polycrystalline anatase films are synthetized via pulsed laser deposition, followed by vacuum annealing. For films thick 50-200 nm, the electrical resistivity is ~8×10-4-1×10-3 Ωcm and charge carrier density increases with doping content while mobility decreases. Below a thickness of 20 nm the electrical properties partially deteriorate, but still conductive ultra-thin films can be obtained down to 5 nm. The optical response changes with Ta addition, i.e. the absorption band in the UV range blue-shifts, according to the Moss-Burstein effect, while absorption in the IR increases because of free carriers. Finally, we provide estimates of the effective mass and the plasma energy range in the IR. The fine tunability of the optoelectrical properties of Ta:$TiO_2$ films makes them suitable for devices as transparent conductive components and for photonic or plasmonic applications in the visible and IR range.

## Introduction

Transparent conducting oxides (TCOs) have been attracting much attention because of their ability to combine good electrical properties and transparency in the visible region.[1] These peculiar properties allow TCOs to be employed as electrodes in optoelectronic devices, such as solar cells,[2] photodetectors,[3] flexible displays,[4] and light-emitting diodes.[5] The most employed TCO for consumer products is Sn-doped indium oxide (ITO) because of its high optical transparency in the visible range (i.e. >80%) and very low resistivity (1-2×$10^{-4}$ Ωcm);[6] however, the limited availability of In has been driving the research toward alternative materials, including Al-doped ZnO (AZO) and $TiO_2$-based TCOs.[1,7–9] $TiO_2$ is widely investigated in the literature for energy conversion and photocatalytic applications because of its activity, low cost, non-toxicity and chemical stability;[10] it is commonly employed as the photoanode in dye sensitized solar cells thanks to its favourable electronic band alignment with the active component of the cell, and is a promising photo-absorbing material for photovoltaics and photocatalysis.[11–13]

The conductivity of $TiO_2$ can be improved by n-type doping, which consists in substitutional dopant atoms whose excess electrons are transferred to the conduction band of the matrix.[14] Among the $TiO_2$ allotropes, anatase is the most attractive because of its band gap equal to 3.2 eV and the low conduction-band effective mass, around 1 $m_e$ (although the actual value depends on the direction due to the anisotropy of the structure),[15,16] while the energy gap and the effective mass of the rutile phase are about 3.0 eV and 20 $m_e$, respectively.[10] Nb- and Ta-doped anatase have been studied as $TiO_2$-based TCOs, in particular Ta is reported to have both higher solubility and lower effective mass than Nb, which favors the mobility.[16] Experimentally, both Nb- and Ta-doped anatase films epitaxially grown via pulsed laser deposition (PLD) showed very similar resistivity around 2-3×10-4 Ωcm,[17,18] suggesting almost identical electrical conduction mechanisms, with a resistivity comparable to commercial polycrystalline ITO. However, the resistivity of Nb and Ta:$TiO_2$ polycrystalline films is typically higher than that of epitaxial films and strongly dependent on the film structural properties, which implies a correlation with the synthesis conditions. Moreover, the electrical properties were demonstrated to be dependent on the oxygen stoichiometry and, in particular, the optimal values occurred for

[a] Micro- and Nanostructured Materials Laboratory, Department of Energy, Politecnico di Milano, via Ponzio 34/3, 20133 Milano, Italy.
[b] OptMatLab, Dipartimento di Fisica, Università di Genova, via Dodecaneso 33, I-16146, Genova, Italy.
[c] Laboratory of Supramolecular and Bio-Nanomaterials, Department of Chemistry, Materials, and Chemical Engineering "Giulio Natta", Politecnico di Milano, Via L. Mancinelli 7, 20133 Milano, Italy.
[d] Center for Nanoscience and Technology – IIT@Polimi, via Giovanni Pascoli 70/3, 20133 Milano, Italy
[e] CNR-SPIN, C.so Perrone 24, 16152 Genova, Italy
[f] Department of Physics, Politecnico di Milano, piazza Leonardo da Vinci 32, 20133 Milano, Italy
*Corresponding author
Electronic Supplementary Information (ESI) available.

a specific amount of oxygen deficiency.[19] Indeed, the calculated formation energy of $Nb_{Ti}$ and $Ta_{Ti}$ is very low under Ti-rich/O-poor conditions,[14] while oxygen-rich conditions promote electron acceptor defects, namely cationic vacancies and interstitial oxygen atoms, which reduce the conductivity.[15,20,21]

Mazzolini et al. performed a study on the structural, electrical, and optical properties of Ta:$TiO_2$ with 5% at. Ta nominal content, while the oxygen content of the films was varied during the synthesis.[15] In particular, Ta:$TiO_2$ films with thickness around 200 nm were obtained via PLD, which allows one to control the oxygen partial pressure during film deposition by means of gas mass flow, enabling in turn the tuning of oxygen stoichiometry in the deposited films. After deposition, a thermal treatment in vacuum is required in order to obtain films with the anatase crystalline phase. The study revealed a dependency of the electrical and optical properties on the oxygen partial pressure during deposition and an optimal condition was identified.

Starting from this knowledge, in this work the structural, optical and electrical properties of thin and ultra-thin Ta-doped $TiO_2$ films are investigated as a function of thickness (from 200 down to 10 nm) and Ta content (5 and 10 % at.) and compared with bare $TiO_2$. Such a systematic study is presently lacking, despite being essential for a better comprehension of the material behaviour in view of possible applications where size-dependent effects can become relevant. Indeed, the thickness can have a key role for TCOs in optoelectronic devices, where the highest possible transparency in the visible range should be combined with the desired electrical resistivity and charge carrier density. In addition, thin and ultra-thin TCO films have been proposed for their implementation in sub-wavelength nano-optics structures,[22] replacing metals, which present a percolation threshold when deposited on silicon or glass substrates and have poor compatibility with microfabrication foundry processes, while extending the applicable wavelength range toward the mid- and near-infrared range.[23–25]

In detail, homogeneous and compact polycrystalline Ta:$TiO_2$ thin films in the anatase phase were deposited on silicon and glass substrates with different Ta content and thickness, down to ultra-thin layers. The electrical characterization demonstrates marginal changes for films in the 50-200 nm thickness range. The electrical resistivity is between $8\times10^{-4}$ and $1\times10^{-3}$ Ωcm for both Ta contents, while the charge carrier density increases almost linearly with the Ta concentration and concurrently the Hall mobility decreases. For films thinner than 20 nm the electrical properties start to deteriorate but still conductive 10 nm-thick films were obtained. The optical properties are extracted from ellipsometric measurements, combined with transmittance and reflectance spectra, and the effect of Ta-doping is explored from the near-IR to the UV range. Finally, material properties of interest were calculated starting from experimental results in terms of optical band gap, effective mass, and plasma energy in view of potential optoelectronic applications.

## Results

### Morphology and structure

Ta:$TiO_2$ thin films with nominal content of Ta= 5, 10% at. and bare $TiO_2$ films were deposited via PLD at a background pressure of 1 Pa $O_2$, followed by vacuum thermal treatment. Such a background oxygen pressure during deposition was carefully chosen to optimize the electrical properties of the resulting Ta:$TiO_2$ films (Figure S1), corresponding to the lowest resistivity and highest carrier mobility. Figure 1 shows the SEM cross-section images of vacuum-annealed Ta(5%):$TiO_2$ thin with different thickness, i.e. from 200 down to 20 nm. Films present a compact morphology, both for Ta(10%):$TiO_2$ and bare $TiO_2$ thin films. The estimation of the amount of tantalum in Ta:$TiO_2$ via EDS is about 4.5 and 9% at. for films with nominal Ta content of 5 and 10%, respectively, as expected for PLD depositions that preserve the cationic ratio of the ablated material.

Optical microscopy allowed for the surface investigation of films with thickness in the range of 50-200 nm, while thinner films did not provide any sizeable optical contrast. The average lateral size of the polycrystalline domains was measured to be 15-20 μm for Ta(5%):$TiO_2$ and 25-30 μm for Ta(10%):$TiO_2$ films. This difference can be ascribed to the different laser fluence employed during film depositions. The surface images of

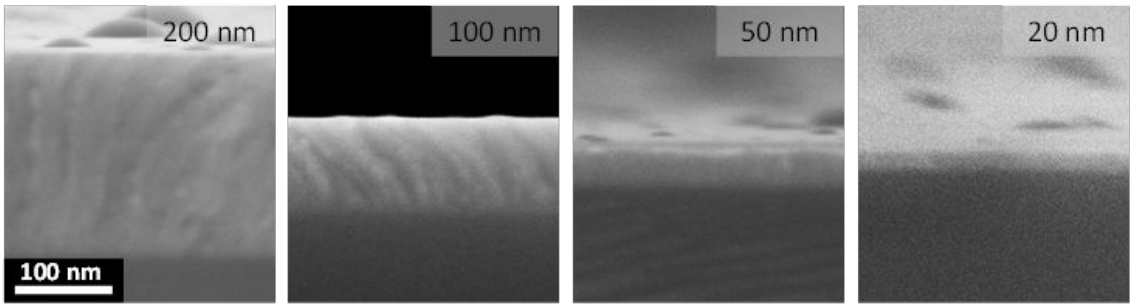


Figure 1 - SEM cross-section micrographs of vacuum-annealed Ta(5%):$TiO_2$ films deposited on a Si substrate with different thickness, i.e. 200, 100, 50 and 20 nm.

Ta(5%):$TiO_2$ and Ta(10%):$TiO_2$ 200 nm-thick films captured by using polarized-light microscopy are shown in Figure S2.

The structural characterization of the films was performed via XRD. Figure 2 shows the resulting diffractograms as a function of the Ta content for vacuum-annealed films with nominal thickness equal to 200 nm, compared to vacuum- and air-annealed $TiO_2$. An initial investigation of the XRD patterns highlights that all the analysed films reveal only the presence of crystalline anatase phase, while no rutile phase is observed. In addition, in both the tantalum-doped films neither the presence of tantalum oxide ($Ta_2O_5$) phases nor metallic tantalum aggregates are detected, suggesting the formation of homogeneous solid solutions.[26]

In all the analysed films the more intense diffraction peak is the one associated with the (101) surfaces. This behaviour can be explained since it is known that anatase thin films grown on amorphous substrates preferably form [101]-oriented polycrystalline systems, since those possess the lowest surface energy.[27,28] Interestingly, in both the Ta-doped films the relative intensity of the (101) peak is higher than in the $TiO_2$ samples, suggesting that in the Ta-doped systems the effect of the doping could induce a preferential direction towards the lowest surface energy, namely the [101].

The atomic radius of Ta is slightly larger than the atomic radius of Ti, 145 and 140 pm, respectively, and, although the percentage of Ta is relatively low, this could introduce lattice distortions in the samples, which lead to a shift of the measured XRD peaks, as shown for the (101) peak in the inset of Figure 2. A whole profile fitting performed on the films allows one to calculate the lattice parameters of the tetragonal cell of the $TiO_2$ anatase phase, demonstrating a variation of the length for the *a* and *c* axes in relation to the Ta content. Specifically, in the Ta-doped films both the *a* and *c* axes are longer than in the pristine $TiO_2$ films and their length increases with the Ta content (see Table 1).

Table 1 Lattice parameters (*a* and *c*), cell volume and mean crystalline domain size ($\tau$) of 200 nm-thick films of air- and vacuum-annealed $TiO_2$, Ta(5%):$TiO_2$ and Ta(10%):$TiO_2$.

| Sample | *a* [Å] | *c* [Å] | Volume [Å$^3$] | $\tau$ [nm] |
|---|---|---|---|---|
| $TiO_2$-air | 3.634 | 9.590 | 126.680 | 53 |
| $TiO_2$ | 3.783 | 9.483 | 135.735 | 56 |
| Ta(5%):$TiO_2$ | 3.793 | 9.498 | 136.646 | 76 |
| Ta(10%):$TiO_2$ | 3.793 | 9.542 | 137.299 | 68 |

The presence of the doping also affects the crystallite size along the direction normal to the film surface, which can be calculated by using the Pawley method on diffractograms as described in the Experimental section, in fact both the Ta-doped films show a slightly larger mean domain size than the undoped $TiO_2$ films. In particular, Ta(5%):$TiO_2$ films display a larger domain size equal to 76 nm, while in Ta(10%):$TiO_2$ this reduces to 68 nm. Interestingly, the different annealing procedure, namely in vacuum or air, on the undoped $TiO_2$ films does not produce a marked influence on the mean crystallite domain size that remains almost unchanged (i.e. 53 nm and 56 nm for air- and vacuum annealed $TiO_2$ respectively, see Table 1), while the lattice parameters and the cell volume show more notable differences, as already observed in the literature.[15]

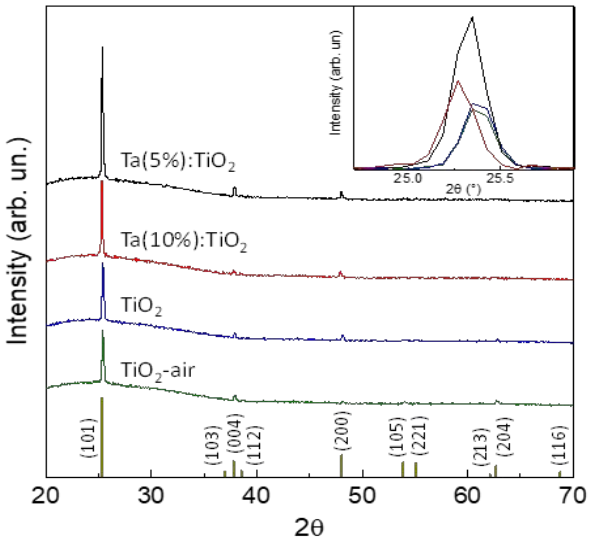


Figure 2 - XRD diffractograms of air- and vacuum-annealed $TiO_2$, Ta(5%):$TiO_2$ and Ta(10%):$TiO_2$ films with nominal thickness of 200 nm. The inset shows a magnification of the (101) peak. The characteristic peaks of the anatase phase are highlighted on the bottom.

Raman spectroscopy of Ta:$TiO_2$ has been carried out for all films down to 10 nm thickness. Figure 3a shows the Raman spectra of vacuum-annealed Ta(5%):$TiO_2$ thin films; all spectra display the Raman peaks of the anatase phase, while no presence of $Ta_2O_5$ or other $TiO_2$ polymorphs is detected, confirming the XRD results. In particular, the $E_g(1)$, $B1_g(1)$, $B1_g(2)$ superimposed to the $A1_g$ and $E_g(3)$ peaks of the anatase phase are evident around their nominal values, i.e. 144, 399, 519, 513, and 638 cm$^{-1}$ for the thickest films (i.e. 75-200 nm).[29,30] On the other hand, for thicknesses in the 10-50 nm range only the $E_g(1)$ and $E_g(3)$ peaks are evident, probably because of the poor signal-to-noise ratio.[31] Raman spectra of Ta(10%):$TiO_2$ films show the same trend as described for the 5% Ta content (see Figure S3).

The Ta content also affects the position of the $E_g(1)$ peak, as demonstrated in Figure 3b; for 200 nm films, the $E_g(1)$ peak shifts from 144 cm$^{-1}$ to 152 and to 155 cm$^{-1}$ for Ta(5%):$TiO_2$ and Ta(10%):$TiO_2$, respectively, while the peak FWHM broadens from about 10 to 13-14 cm$^{-1}$. This trend has been already observed in the literature and associated to a correlation between the $E_g(1)$ peak position and the measured charge

carrier density, independently of the type and amount of extrinsic doping, or the specific deposition and annealing conditions.[32] Figure 3c highlights the evolution of the $E_g(1)$ peak position as a function of the film thickness. At fixed Ta content, the $E_g(1)$ energy does not significantly depend on the thickness, at least down to 20 nm (in agreement with the measured charge carrier density, see next section). On the other hand, for 10 nm-thick films the $E_g(1)$ energy shifts for both Ta contents, namely to 147 and 150 $cm^{-1}$, respectively, while the peak FWHM increases up to 17-18 $cm^{-1}$. This behaviour can be associated to a larger film defectivity, size confinement as well as a smaller charge carrier density.[29]

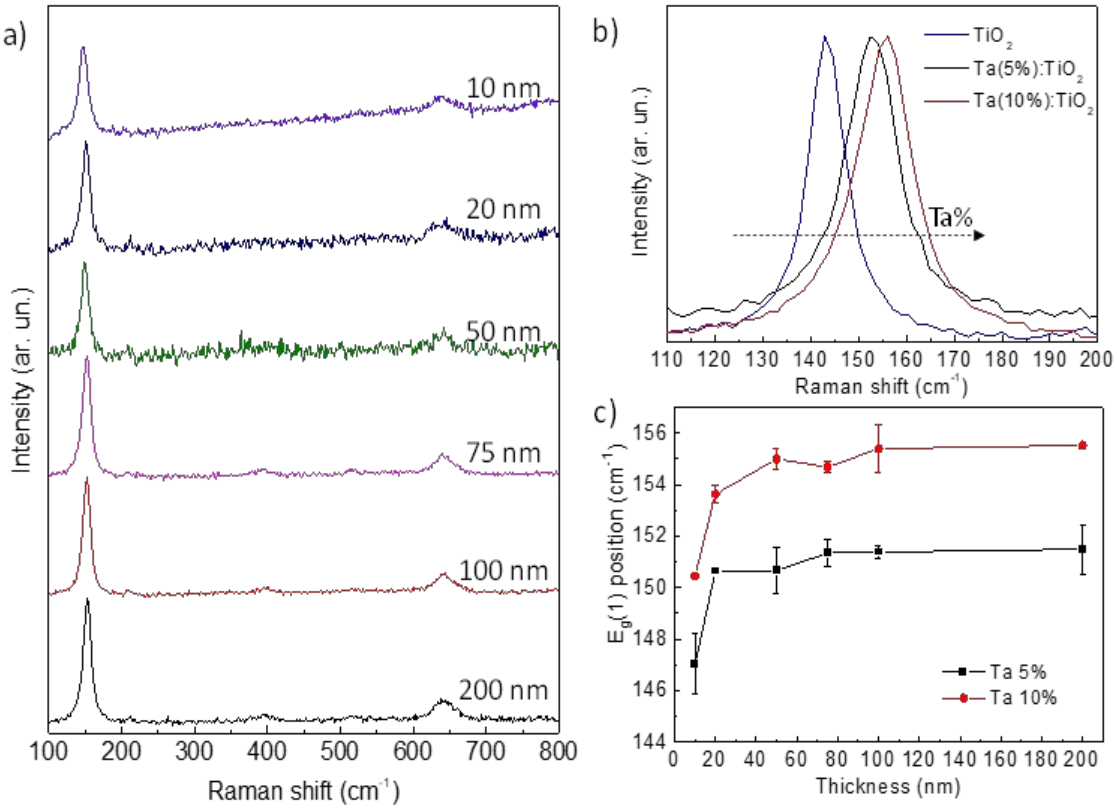


Figure 3 - (a) Raman spectra of Ta(5%):$TiO_2$ films with different thicknesses, i.e. from 10 up to 200 nm; (b) magnification of the $E_g(1)$ peak of Raman spectra of films with different Ta content (5, 10 %at. and bare $TiO_2$) with a thickness of 200 nm; (c) centre energy of the fitted $E_g(1)$ peak as a function of the film thickness for different Ta contents.

**Electrical properties**

Figure 4 reports resistivity ($\rho$), charge carrier density ($N_e$), and Hall mobility ($\mu$) measured for Ta:$TiO_2$ specimens as a function of thickness (from 10 to 200 nm) and Ta content. Measurements on bare $TiO_2$ films (thickness 50, 100 and 200 nm), synthetized and annealed in vacuum under the same conditions as the Ta:$TiO_2$ films, are reported as reference (blue triangles). Notably, stoichiometric $TiO_2$ is expected to be insulating, as confirmed by measurements on PLD $TiO_2$ films annealed in air (for which the resistivity was too high for the accessible range of our experimental setup). In this case, $TiO_2$ films obtained by PLD at 1 Pa $O_2$ after vacuum annealing treatment display a resistivity of about $10^{-2}$ Ωcm and charge carrier density of 5-7×$10^{19}$ $cm^{-3}$. This behaviour can be associated to a $TiO_2$ anatase phase with oxygen vacancies induced by the atmospheric conditions during deposition and annealing, which represent an effective doubly negative charged donor state.[15,33]

For Ta:$TiO_2$ films the resistivity is up to one order of magnitude lower than bare $TiO_2$ for both Ta contents, i.e. down to $10^{-3}$ Ωcm, because of conduction electrons from the Ta active dopants (see Figure 4a). Focusing on Ta(5%):$TiO_2$ films, the resistivity is almost constant for thicknesses ranging from 200 down to 50 nm, with a slight increase from 8×$10^{-4}$ up to 1×$10^{-3}$ Ωcm, while a more evident increment occurs for 20 nm-thick film, where the resistivity reaches 3×$10^{-3}$ Ωcm. The same trend is found for Ta(10%):$TiO_2$, where resistivity is around 1×$10^{-3}$ Ωcm for films in the 50-200 nm thickness range, while it increases to about 2×$10^{-3}$ Ωcm for 20 nm-thick films.

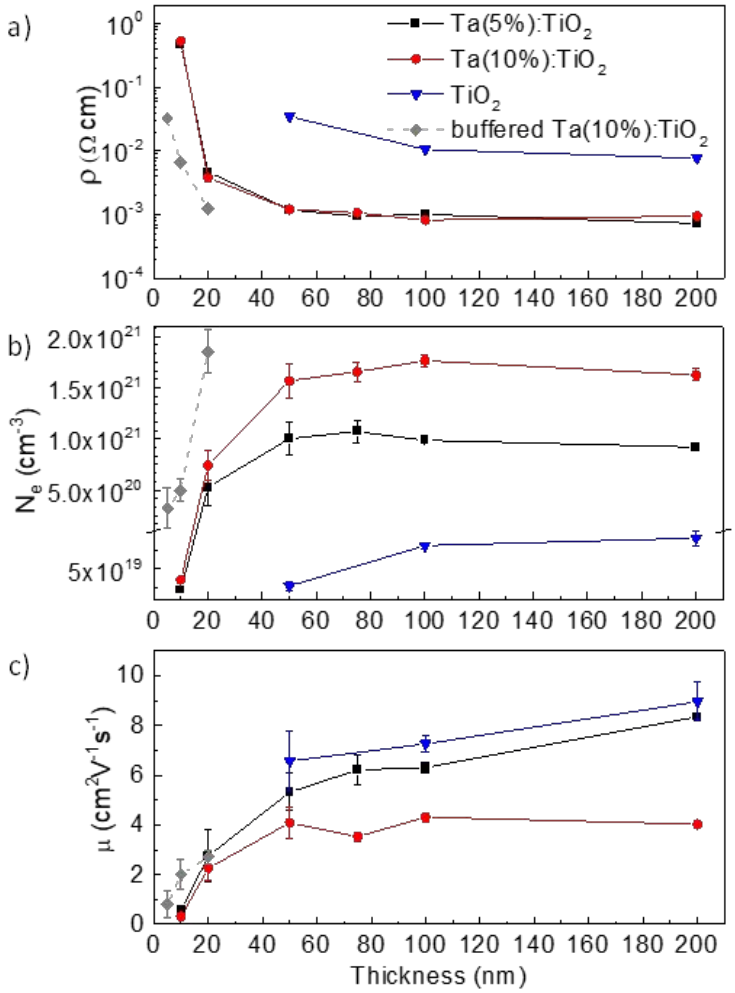


Figure 4 - (a) Resistivity ($\rho$), (b) charge carrier density ($N_e$) and (c) Hall mobility ($\mu$) as a function of film thickness (from 10 to 200 nm) and Ta content: Ta(5%):$TiO_2$ (black squares), Ta(10%): $TiO_2$ (red circles), bare $TiO_2$ (blue triangles) and Ta(10%):$TiO_2$ ultra-thin films deposited on a buffer layer of insulating 50 nm-thick $TiO_2$ (grey rhombus).

For both doping contents, the charge carrier density does not significantly vary with thickness down to 50 nm (Figure 4b). Moreover, the carrier density Ne of the Ta(10%):$TiO_2$ films is almost twice that of Ta(5%):$TiO_2$, with average values in the 50-200 nm thickness range of about $1.65\times10^{21}$ and $9.95\times10^{20}$ $cm^{-3}$, respectively. For 20 nm-thick films the charge carrier density is slightly smaller than in thicker films for both Ta contents, but Ta(10%):$TiO_2$ film still show a higher value than Ta(5%):$TiO_2$ ($7.4\times10^{20}cm^{-3}$ against $5.3\times10^{20}cm^{-3}$, respectively). These results indicate that the charge carrier density increases proportionally with Ta content in a condition of high dopant activation efficiency (calculated equal to 74% and 68% for Ta(5%):$TiO_2$ and Ta(10%):$TiO_2$, respectively, with respect to the measured EDS concentrations) as observed for thicker films as well.[18,32] In addition, the measured charge carrier density is in good agreement with the observed energy shift of the $E_g(1)$ Raman peak, which increases with Ta content and decrease for films thinner than 20 nm.

For 200 nm-thick films, the Ta content significantly affects the Hall mobility (Figure 4c). Indeed, while the mobility μ measured for Ta(5%):$TiO_2$ is almost to the same as for bare $TiO_2$ (i.e. around 8 $cm^2V^{-1}s^{-1}$), the Hall mobility of Ta(10%):$TiO_2$ is reduced by a factor of about 2. This behaviour is mostly related to the higher concentration of ionized impurities in the crystal lattice, which affects electron scattering, as well as to the higher probability of carrier-carrier and carrier-defect interaction at larger values of $N_e$.[8,32] Moreover, the Hall mobility for Ta(5%):$TiO_2$ decreases gradually from about 8 down to about 5 $cm^2V^{-1}s^{-1}$ for thicknesses varying from 200 down to 50 nm, while it reaches a value of about 1.5 $cm^2V^{-1}s^{-1}$ for 20 nm-thick films. On the other hand, the mobility remains almost constant and around 4 $cm^2V^{-1}s^{-1}$ for Ta(10%):$TiO_2$ films down to 50 nm dropping to about 2 $cm^2V^{-1}s^{-1}$ for 20 nm-thick films. This trend can be related to the reduction of the characteristic grain size, as well as to the presence of defects such as grain boundaries or dislocations affecting the mobility.[34] Indeed, the mean crystalline domain size calculated from XRD measurements (76 nm and 68 nm for Ta(5%):$TiO_2$ and Ta(10%):$TiO_2$, respectively) confirms that the higher Hall mobility of Ta(5%):$TiO_2$ is also accompanied by larger grains; moreover, a significant decrease of $\mu$ for decreasing thicknesses is expected for

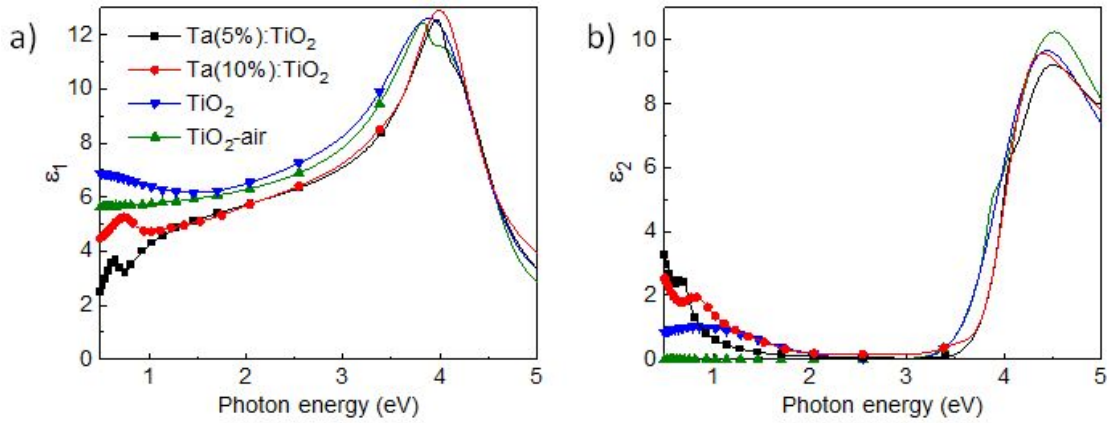


Figure 5 - (a) Real and (b) imaginary parts of the dielectric constant of Ta:$TiO_2$ films with different doping levels (5, 10% at.) compared with bare vacuum-annealed ($TiO_2$) and air-annealed ($TiO_2$-air).

thicknesses much smaller than the calculated mean domain size, such as in 20 nm-thick films, where crystalline grains cannot develop completely.

On the other hand, 10 nm-thick films display a radically different electrical behaviour, almost independent of the Ta content. Indeed, for both Ta(5%):$TiO_2$ and Ta(10%):$TiO_2$ 10 nm-thick films, the resistivity measured is about 0.5 Ωcm, i.e. more than two orders of magnitude higher than thicker Ta:$TiO_2$ films (see Figure 4a). Hall effect measurements on these films were less reliable and reproducible, probably because of the higher resistance of the film as well as the difficulty to measure such a thin film with our setup. The measured charge carrier density was 2.3 and $3.5\times10^{19}$ $cm^{-3}$ for 5 and 10% at. Ta content respectively, namely around 2 orders of magnitude smaller than thicker films (Figure 4b). At the same time, the Hall mobility drops by one order of magnitude with μ=0.56 $cm^2V^{-1}s^{-1}$ for Ta(5%):$TiO_2$ and μ=0.31 $cm^2V^{-1}s^{-1}$ for Ta(10%):$TiO_2$ (Fig 4c). This behaviour can be explained with the presence of defects at the film surface and at the interface with the substrate, causing electron trapping and scattering that become dominant in ultra-thin films with a thickness below 20 nm, together with the smaller domain size as discussed before.[34–36]

The electrical properties of ultra-thin Ta:$TiO_2$ films can be enhanced by exploiting an appropriate buffer layer that improves the wettability and the interface quality and reduces the high defectivity promoted by growing the films on lattice-mismatched substrates (e.g. glass and silicon).[36–40] In this case, we investigated the effect of a 50 nm-buffer layer of polycrystalline stoichiometric $TiO_2$ (air-annealed) in anatase phase on the growth of Ta(10%):$TiO_2$ films with 5, 10 and 20 nm thickness. The $TiO_2$ buffer layer alone is insulating and the measured electrical properties of the buffered films are reported in Figure 4 (grey diamonds), showing an improvement for both 10 and 20 nm thick films. In particular, the buffered 20 nm-thick film displays a decrease in resistivity and an increase in charge carrier density up to values similar to the unbuffered Ta(10%):$TiO_2$ films with 50-200 nm thickness, while buffered 10 nm-thick films improve all the electrical properties to values similar to the unbuffered 20 nm-thick film. Finally, since the buffer layer favours a better wettability of the growing film onto the substrate, we were able to deposit conductive Ta(10%):$TiO_2$ films with a thickness as low as 5 nm, which is unaffordable by depositing directly on glass, even though the electrical properties show a deterioration. These results highlight the possibility to design devices with ultra-thin conductive films, replacing metals which present a percolation threshold.[22]

**Optical properties**

Ellipsometric measurements were performed on Ta:$TiO_2$ films with 200 nm nominal thickness, grown on Si substrates covered by a few-nm thick native $SiO_2$ layer as described in the experimental section. The corresponding $\psi$ and $\Delta$ measurements are shown in Figure S5 of the supporting information. Figure 5a,b reports the real ($\varepsilon_1$) and the imaginary ($\varepsilon_2$) part of the dielectric functions extracted by means of the optical model described in the experimental section. The results for Ta:$TiO_2$ with Ta content 5 and 10% at. are compared to bare $TiO_2$ with the same nominal thickness, both air-annealed and vacuum-annealed. The corresponding refractive index and extinction coefficient are reported in Figure S5.

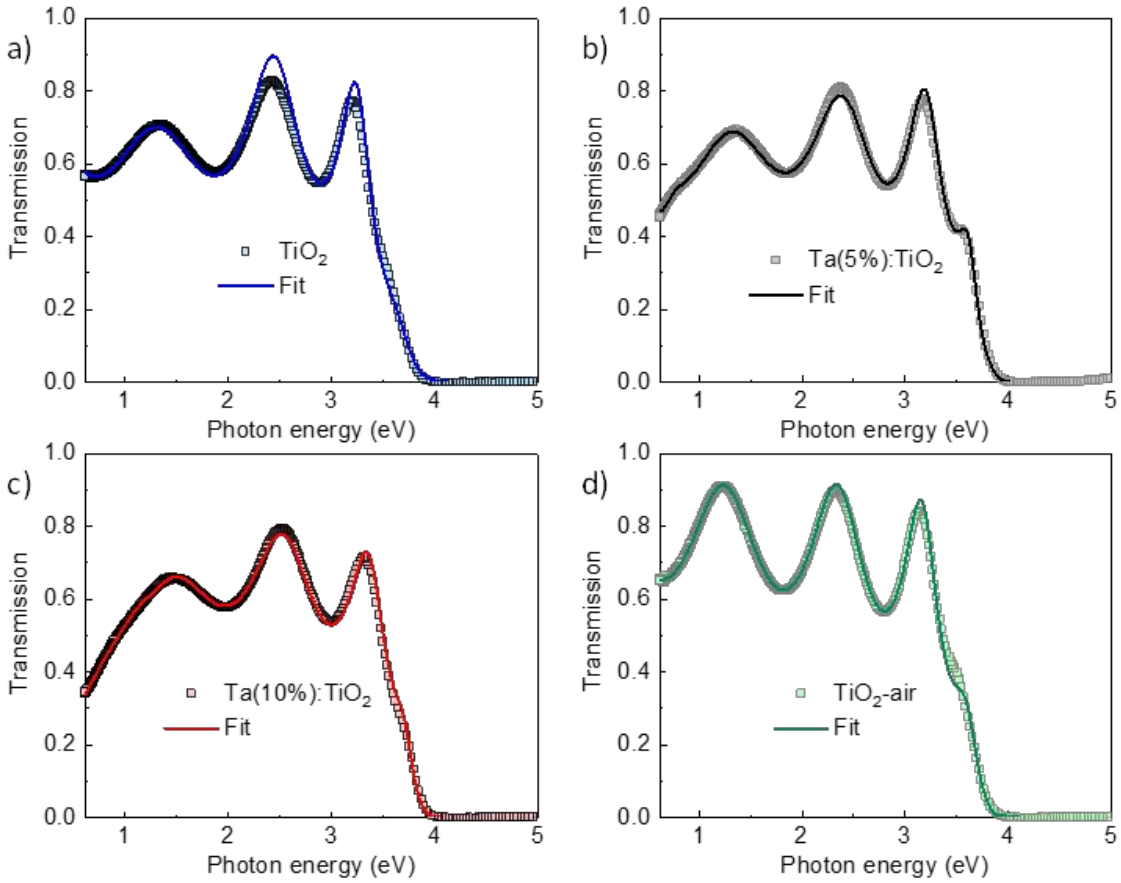


Figure 6 - Transmission measurements of vacuum-annealed (a) $TiO_2$, (b) Ta(5%):$TiO_2$, (c) Ta(10%):$TiO_2$ and (d) air-annealed $TiO_2$ films of 200 nm thickness, grown on soda-lime glass substrates. Squares represent the experimental data while lines the theoretical fit, as extracted from ellipsometry measurements.

For the real part ($\varepsilon_1$, Figure 5a), air-annealed $TiO_2$ shows two humps in the high-energy region (3.5-4.5 eV), while vacuum-annealed $TiO_2$ shows a unique band in the same range. In the visible range, $\varepsilon_1$ decreases with decreasing energy for both air- and vacuum-annealed $TiO_2$ with almost the same slope. For both samples, $\varepsilon_1$ values are in accordance with those reported in the literature for the anatase phase over the investigated spectral range, with a maximum around 12.5 at 3.8-3.9 eV and a value between 6 and 9 in the visible range (1.7-3.3 eV).[41–44] In the near-IR range, $\varepsilon_1$ is flat for air-annealed $TiO_2$, while its value increases for decreasing energy for vacuum-annealed $TiO_2$. On the other hand, Ta doping leads to blue-shifted and narrowed features in the UV range, while the maximum values of $\varepsilon_1$ are close to those of bare $TiO_2$. In the visible range, the $\varepsilon_1$ curves for Ta:$TiO_2$ films almost overlap and decrease as bare $TiO_2$ but at lower values (this behaviour has been already reported by Manole *et al.* for the Nb-doped anatase phase),[45] while in the near-IR range $\varepsilon_1$ decreases, as expected by the free-carrier contribution that sets the plasma frequency in the mid-IR spectral range.

In Figure 5b, $\varepsilon_2$ of air-annealed $TiO_2$ exhibits a band in the UV range associated to optical band gap absorption with a peak around 4.5 eV and a shoulder around 3.8 eV. This shape is associated to the anisotropy of the crystal structure in the anatase phase, which results in optical properties strongly dependent on the polarization direction of the incident light beam. Indeed, the shoulder and the peak are associated to the perpendicular and parallel components (with respect to the *c*-axis) of the dielectric tensor.[41,42,46] Similar to $\varepsilon_1$, also $\varepsilon_2$ shows a single feature in the UV range for vacuum-annealed $TiO_2$ at the same energy as air-annealed $TiO_2$, but with a slightly smaller value. The effect of Ta doping is the shift of the absorption band in the UV towards higher energy values, suggesting a larger optical band gap with respect to bare $TiO_2$ films, due to the Moss-Burstein effect (see next section).[47,48] In the visible range, all $\varepsilon_2$ curves are close to zero, suggesting no absorption as expected for $TiO_2$ and $TiO_2$-based TCOs. In the lower-energy region of the visible range (below 2 eV) and in the near-IR range, $\varepsilon_2$ of air-annealed $TiO_2$ curve is close to zero, while for vacuum-annealed $TiO_2$ it increases to a maximum around 0.84 eV. The different behaviour of vacuum-annealed $TiO_2$ with respect to air-annealed $TiO_2$ in this range can be associated to the oxygen vacancy concentration in the anatase structure (as already discussed in the previous section).[49,50] On the other hand, Ta:$TiO_2$ films show a larger increase of $\varepsilon_2$ in this range, which is again consistent with a prominent plasma response in the mid-IR region. Notably, both Ta:$TiO_2$ films show a peak in this range at 0.68 and 0.82 eV for Ta content of 5 and 10% at., respectively, that correspond to dispersive features in $\varepsilon_1$ curve in the same range.

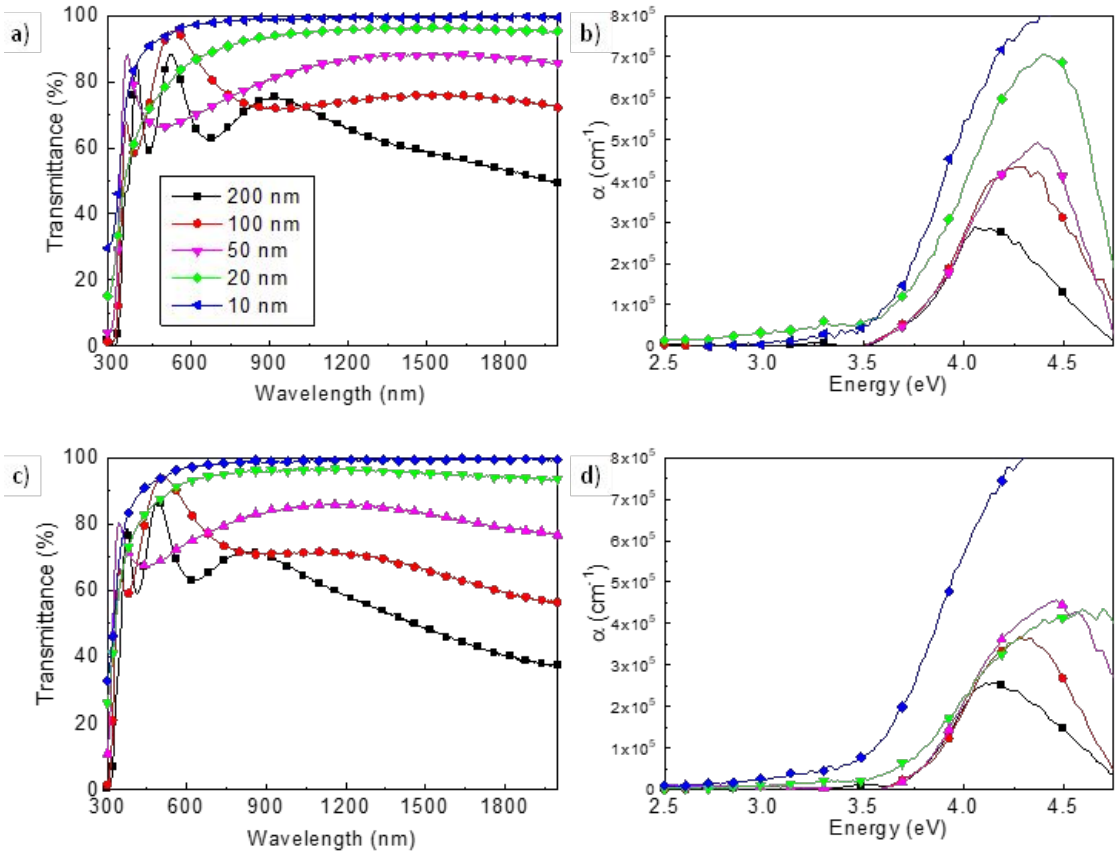


Figure 7 - Optical transmittance and absorption coefficient (α) as a function of thickness (10-200 nm) of (a,b) Ta(5%):$TiO_2$ and (c,d) Ta(10%):$TiO_2$ films; the legend of all images is in figure (a).

Therefore, the optical properties in the near-IR range of both Ta:$TiO_2$ films show an absorptive behaviour associated with the tail of free carrier (plasma) oscillations that come into play below the screened plasma frequency, which sets the onset of conductive behaviour and is expected to blue-shift with charge carrier density,[34,51] as observed comparing Ta(5%) and Ta(10%):$TiO_2$. The explanation of the weak peaks in the near-IR range in $\varepsilon_2$ curves is less straightforward. A tentative hypothesis is the establishment of a strong interaction between plasma oscillation of free carriers and phonons, with a formation of longitudinal optical phonon-plasmon coupled modes. This phenomenon is typical of polar semiconductors and it occurs in the IR dielectric response,[52,53] which can be described by a harmonic oscillator function with Lorentzian line shape.[54] Although Ta:$TiO_2$ is not a polar material, the large carrier density due to Ta doping as well as the large degree of lattice defects could induce an increase in the ionic character of the Ti-O covalent bond.

The optical constants extracted from ellipsometry were directly applied to the modelling of normal-incidence transmission spectra, by allowing only for small adjustments in the oscillator parameters to account for the different soda-lime substrate compared to the silicon one. In Figure 6 experimental data from the transmission measurements are shown (squares) along with the fit data (continuous lines), which are the outcome of the modelling. The respective dielectric constants, refractive index and extinction coefficients that came out of the modelling of this system are shown in Figure S6. Indeed, transmittance spectra confirm the optical behaviour observed with the previous analysis of the dielectric function. For all the spectra, the transmittance goes to zero in the UV range due to interband absorption, while it increases in the visible and near-IR range. The oscillations in this range are due to thin-film interference and related to the film optical path length.[8,55] Vacuum-annealed $TiO_2$ displays lower transmittance intensity than air-annealed $TiO_2$ in the energy range from visible to near-IR associated to absorption by oxygen vacancies, while both Ta:$TiO_2$ films show a stronger decrease in transmittance in the near-IR due to free carrier absorption related to the response of the conduction plasma. Furthermore, the effect of increasing the Ta content is observed as a blue-shift of the absorption edge in the UV range, because of the Moss-Burstein effect, as previously explained.

Figure 7a,c shows optical transmittance spectra as a function of film thickness, from 10 nm up to 200 nm, of Ta(5%):$TiO_2$ and Ta(10%):$TiO_2$ films. Thickness reduction leads to an increase in transmittance in the visible and near-IR range because of the reduced absorption, according to the Lambert-Beer law, while interference fringes change according to the optical path length.[55] This modulation of fringe position is a feature that can be exploited in applications in which TCO films are employed as transparent electrodes and a fine tuning of the film transparency at specific wavelengths is required. The effect of thickness in the UV range is more appreciable looking at the absorption coefficient ($\alpha$), reported in Figure 7 b,d as a

 

function of energy, as evaluated from the Lambert–Beer law (see Experimental section). The absorption coefficient shows the onset of the absorption band, which does not depend on thickness down to 50 nm, while it redshifts for 10 and 20 nm-thick films.

## Discussion

The optical gap ($E_{gap}$) of Ta:$TiO_2$ thin films was calculated by means of a Tauc plot of the absorption coefficient (see Experimental section) and results are reported in Figure 8 as a function of the Ta content and thickness. As a reference, the results of 20, 50 and 200 nm-thick vacuum-annealed $TiO_2$ films are also reported and the calculated band gap is about 3.29 eV, in line with the band gap of the anatase phase, namely 3.2-3.4 eV.[10,43] A very similar value of $E_{gap}$ was obtained for air-annealed $TiO_2$ films.

For the thickest Ta:$TiO_2$ films, i.e. in the 50-200 nm range, $E_{gap}$ increases with the Ta content as a consequence of the Moss-Burstein effect, where free carriers partially fill the conduction band forcing higher energy optical transitions.[47] Indeed, the measured charge carrier density of Ta(10%):$TiO_2$ is almost twice that of Ta(5%):$TiO_2$. Congruently, the average band gap calculated for 50-200 nm $TiO_2$ films doped with 5 and 10% at. of Ta was 3.48 and 3.56 eV, respectively. On the other hand, $E_{gap}$ calculated for 10-20 nm-thick film decreases down to the value expected for an undoped film, in agreement with the trend of the charge carrier density which starts to decrease for 20 nm films, down to a value typical of undoped $TiO_2$ for 10 nm-thick films.

To support this analysis, the optical band gap was calculated from ellipsometric measurements as well. The Tauc plot with $\alpha$ extracted from ellipsometry for 200 nm-thick films gives results in agreement with the previous findings, i.e. 3.28 eV for bare $TiO_2$, as well as 3.46 and 3.53 eV for Ta(5%):$TiO_2$ and Ta(10%):$TiO_2$, respectively.

Another important property for a TCO is the effective mass ($m^*$) of electrons in the conduction band. For the calculation of $m^*$ we used the Drude model, which describes the motion of free electrons moving against a fixed background of positive ions, while the overall lattice potential effect is taken into account by $m^*$:

$$\varepsilon_{n_{Drude}} = 1 - \frac{\omega_P^2}{\omega^2 + i\gamma\omega} \quad (1)$$

$$\omega_P = \sqrt{\frac{N_e q^2}{m^* \varepsilon_0}} \quad (2)$$

where $\omega$ is the photon frequency, $\omega_p$ is the unscreened plasma frequency, which can be extracted from the Drude term in the ellipsometric fitting, $\gamma$ is the damping parameter, $\varepsilon_0$ is the vacuum permittivity, $q$ is the electron charge, and $m^*$ is the effective mass of the charge carriers. By knowing $N_e$ from the electrical characterization, i.e. the charge carrier density measured electrically, the effective mass can be calculated by combining the above equations. For Ta(5%):$TiO_2$, such estimates provide a value for $m^*$=0.82 $m_e$, while for Ta(10%):$TiO_2$ $m^*$=1.89 $m_e$. Theoretical calculations for both Nb- and Ta-doped $TiO_2$ and experimental work on Nb-doped $TiO_2$ indicate an anisotropic effective mass, related to anisotropy of the anatase tetragonal crystal structure.[16,56,57] In particular, theoretical calculations report an orthogonal effective mass ($m^*_x$) and a parallel one ($m^*_z$) with respect to tetragonal axis, which resulted equal to 0.4-0.6 $m_e$ and >3.5 $m_e$, respectively.

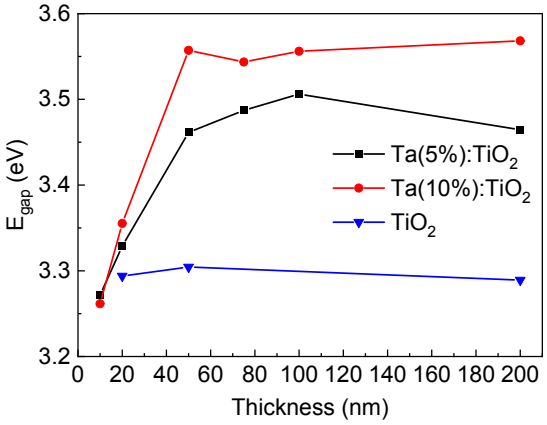


Figure 8 - Optical band gap as a function of thickness (10-200 nm) and Ta content (bare $TiO_2$, 5 and 10% at.) calculated via Tauc plot.

Moreover, calculations predict an increase of $m^*_z$ with the charge carrier concentration.[16] Taking into account that the Ta:$TiO_2$ films reported in this study are polycrystalline, our $m^*$ results are consistent with the reported calculated $m^*_x$ and $m^*_z$ and, at the same time, $m^*$ shows an increase with the Ta content.

An independent estimate of $m^*$ can also be obtained from the optical bandgap increase as a function of the charge carrier density due to the Moss-Burstein effect. In a simplified parabolic-band picture, the shift in the optical band gap follows the equation:[58]

$$\Delta E_{gap} = \frac{\hbar^2}{2m^*}(3\pi^2 N_e)^{2/3} \quad (3)$$

from which we can evaluate the effective mass by knowing $N_e$ from the electrical measurements. The $\Delta E_{gap}$ is calculated by subtracting the optical gap of bare $TiO_2$ (3.29 eV) to that of Ta:$TiO_2$ films (in Figure 8). Since electrical measurements and optical band gap calculations do not show a significant dependence on thickness in the 50-200 nm range, also the effective mass varies marginally with thickness. Indeed, $m^*$ values of 1.7-2.2 $m_e$ and 1.8-2.1 $m_e$ are obtained for Ta(5%):$TiO_2$ films and Ta(10%):$TiO_2$ films, respectively, notably almost the same for both Ta contents. These results are smaller than the effective mass reported in the literature in a previous work on Ta:$TiO_2$ films that employed the same calculation method (i.e. 2.9 $m_e$).[15] However, both calculation procedures (Equation 2 and 3) should be considered only as a qualitative description, since the effect of the non-parabolicity of the bands, which could be accounted for by many-body type interactions, is not considered in the model and the extrapolation of the mid-IR plasma frequency from near-IR ellipsometric data is subject to a certain degree of uncertainty.[59–61] For 20 nm-thick films, larger values of $m^*$ are obtained but the result is affected by the unreliable evaluation of

$\Delta E_{gap}$ due to the transparency of the film, while for 10 nm films $m^*$ cannot be estimated at all.

Finally, we provide an estimate for the screened plasma energy ($E_P$) by revisiting the ellipsometric fitting in the IR and introducing a real-valued offset, indicated as $\varepsilon_\infty$, to take the contribution of the bound electrons of the semiconductor into account. The value of $\varepsilon_\infty$ (equal to about 5.9 and 6.0 for Ta(5%):$TiO_2$ and Ta(10%):$TiO_2$, respectively, in good agreement with the literature[62,63]), allows calculating the screened plasma energy as $E_P = \frac{\hbar\omega}{\sqrt{\varepsilon_\infty}}$. The estimated $E_P$ value is about 0.2 eV for both Ta(5%):$TiO_2$ and Ta(10%):$TiO_2$. It should be noted that this estimate is obtained by extrapolating the ellipsometry model out of the measured range and, thus, must be considered only as a rough indication of the expected plasma energy values. However, these findings can be crosschecked against reflectance and trasmittance spectra collected in the 0.1-1.49 eV range by means of Fourier Transform Infrared Spectroscopy (FTIR, see Figure S7 of the Supporting Information). For both doping levels a reflectivity increase, which is a typical signature of the onset of the plasmonic behavior, is observed in the 0.2-0.3 eV range, in good agreement with the ellipsometric extrapolation. No reflectance drop is instead observed for bare $TiO_2$ film. These $E_P$ values in the near- and mid-IR range are expected for a TCO with charge carrier density of the order of $10^{21}$ $cm^{-3}$. Unfortunately, no straightforward and physically meaningful combination of Drude and Lorentz contributions allows fitting the FTIR data, a fact that reveals a possibly higher level of complexity and will be the subject of future studies.

## Experimental section

PLD was performed in a vacuum chamber equipped with mass flow controllers to tune the partial gas pressure. Ablation was performed with a ns-pulsed laser (Nd:YAG, 2nd harmonic, λ =532 nm) with pulse duration in the 5–7 ns range and repetition rate of 10 Hz. The laser pulses were focused on the target material through a viewport and the target was mounted on a roto-translational manipulator ensuring a uniform ablation. Ta:$TiO_2$ thin films with nominal content of Ta = 5, 10% at. were grown by ablating 2-inch targets of $Ta_2O_5$:$TiO_2$ with molar ration equal to 0.025:0.975 and 0.05:0.95, respectively (99.99% pure, provider “Testbourne Ltd”), while pure $TiO_2$ films were obtained from a 99.9% pure $TiO_2$ target (provider “Kurt J. Lesker”). The laser fluence ($F$) on the target was set at 2.27 J/$cm^2$ for the deposition of $TiO_2$ and Ta(5%):$TiO_2$, while F=2.73 J/$cm^2$ was employed for Ta(10%):$TiO_2$. Depositions were performed at room temperature and in a pure $O_2$ background at the pressure of 1 Pa. The employed substrates were Si (100) and soda-lime glass cleaned in ultrasonic bath with isopropanol and mounted on a rotating sample holder at a fixed target-to-substrate distance of 50 mm. Thin films with different nominal thickness, from 10 to 200 nm, were deposited by varying the deposition duration and the actual thickness values were evaluated by means of a field emission scanning electron microscopy (FEG-SEM, Zeiss SUPRA 40) on samples grown on silicon. The deposition rate is related to the laser fluence and was estimated around 11 nm/min for $TiO_2$ and Ta(5%):$TiO_2$ and 18 nm/min for Ta(10%):$TiO_2$. The FEG-SEM microscope is equipped with an Oxford Instruments Si(Li) detector for energy-dispersive X-ray spectroscopy (EDS), which was employed in this work to estimate the tantalum atomic percentage (at.%) with an accelerating voltage of 10 kV.

All the as-deposited $TiO_2$-based thin films were amorphous, therefore post deposition annealing treatments in a vacuum atmosphere (p < 4 × 10−5 Pa) in a homemade furnace at 550 °C (10 °C/min ramp, 1 h dwell) were employed to obtain polycrystalline anatase films, according to previous studies.[64]

The thin film surfaces were investigated by means of optical microscopy (Leitz orthoplan-pol). Structural characterization was carried out by X-ray diffraction (XRD) and Raman Spectroscopy. XRD patterns were collected using a Bruker D8 Advance X-ray diffractometer at 293 K (Cu Kα1 radiation - 1.5406 Å). The measurements were carried out in a Bragg–Brentano geometry with a step–scan technique and a 2θ range of 10–70°. Data were acquired by a Lynx Eye detector in continuous scanning mode with a step size of 0.038° and a time step of 0.15 s. The mean crystallite size domain (τ) along the film growth direction and the lattice parameters of the samples were determined by using the full profile fitting Pawley method.[65] The Pawley method was carried out using the program-suite TOPAS from Bruker. Raman spectra were collected using a Renishaw InVia micro Raman spectrometer with an argon ion laser (514 nm), a laser power at the sample of 0.13 mW and a spectral resolution of about 3 $cm^{-1}$.

Electrical characterization and Hall effect measurements were performed on $TiO_2$ and Ta:$TiO_2$ films deposited on soda-lime glass in the four-point probe configuration with a Keithley K2400 Source/Measure Unit as a current generator (from 100 nA to 10 mA), an Agilent 34970A voltage meter, and a 0.57 T Ecopia permanent magnet.

Optical transmittance ($T$) and reflectance ($R$) spectra in the spectral range 250−2000 nm were evaluated on samples deposited on soda-lime glass with a UV−vis−NIR PerkinElmer Lambda 1050 spectrophotometer with a 150 mm diameter integrating sphere. All the acquired spectra were normalized with respect to the glass substrate contribution. The absorption coefficient ($\alpha$) was evaluated from the Lambert−Beer law $\alpha = -1/d\,[T/(1-R)]$, where $d$ is the film thickness. The optical energy gap ($E_{gap}$) was calculated by means of a Tauc plot, where $(\alpha h\nu)^n$ versus $h\nu$ was plotted in the proximity of the absorption onset of the films in the UV and the exponent n was chosen equal to 0.5 because of the indirect band gap of anatase; $E_{gap}$ was extrapolated with the intercept in the energy axis using a linear fit.

Fourier Transform Infrared Spectroscopy (FTIR) was performed both in transmission and reflection geometry with a commercial instrumentation (INVENIO-R byBruker), employing a halogen lamp emitting in the near-IR and a globar source emitting in the mid-IR spectral range, together with a mercury cadmium

telluride (MCT) detector to acquire spectra in the 0.1-1.49 eV spectral range. The beam incidence on the sample is almost normal (about 10° incidence angle) and the diameter of the beam in the focus is about 1 mm. For these measurements, films with a thickness of 670 nm (in order to have enough transmittance contrast in the measured range) were deposited on $CaF_2$ substrates.

Spectroscopic Ellipsometry (SE) was perfomed by means of a J.A. Woollam V-VASE ellipsometer (0.5-5.05 eV energy range, incidence angle of 60°). The analysis involves evaluating the ellipsometric angles ψ(λ) and Δ(λ), defined as $\frac{r_p}{r_s} = \tan \Psi \cdot e^{i\Delta}$, where $r_{p(s)}$ are the Fresnel reflection coefficients for *p(s)*-polarized radiation. The measurement of amplitude and phase-related quantities adds a degree of precision, useful in deducing the dielectric function of materials, even with complex nanoscale morphology.[66] From the optical point of view, the system was modelled as a stack of dielectric layers, each characterized by its thickness and complex dielectric function. The optical response of the system was calculated assuming Fresnel boundary conditions at the interface between the layers. Bottom to top, the model included: i) a semi-infinite Si substrate, ii) a native oxide layer, iii) the Ta:$TiO_2$ film and iv) a roughness layer (the latter modelled as a Bruggemann effective-medium layer composed by 50% of Ta:$TiO_2$ and 50% of voids). For the modelling of the optical properties of Ta:$TiO_2$ films we employed a combination of Lorentz, Lorentz-gaussian and so-called PSEMI oscillators, along with a Drude-type contribution to take the doping-induced free carriers into account. PSEMI oscillators are parameterized functions widely employed to model the optical response of crystalline semiconductors.[67,68] The oscillator parameters of the undoped $TiO_2$, and the Ta:$TiO_2$, layer, as well as the thickness of all the optical layers were carefully fitted in order to achieve the best agreement between the experimental data and the simulated SE spectra. The thickness of the $SiO_2$ native oxide was assessed by SE measurements on a bare substrate and resulted around 2 nm.

## Conclusions

In this work, Ta-doped $TiO_2$ thin films were investigated as a function of the Ta content (5 and 10% at.) and of the thickness (in the 10-200 nm range), focusing on their structural, electrical, and optical properties, while comparing the results with bare $TiO_2$. Homogeneous and compact Ta:$TiO_2$ films were synthetized via pulsed laser deposition followed by a vacuum thermal treatment, obtaining poly-crystalline films in the anatase phase with preferential growth along the (101) direction.

The effect of the Ta content on the electrical properties is found to depend on the thickness. For films in the 50-200 nm range, the measured resistivity is between $8\times10^{-4}$ and $1\times10^{-3}$ Ωcm for both Ta contents, while the charge carrier density Ne increases proportionally to the Ta content, suggesting a condition of high dopant activation efficiency. On the other hand, the Hall mobility decreases with the Ta content due to a higher concentration of ionized impurities in the crystal lattice, which affects the electron scattering at higher values of $N_e$. The electrical properties deteriorate for films thinner than 20 nm almost independently of the Ta content, but still conductive films are obtained for 10 nm-thick films (with a resistivity of about 0.5 Ωcm). In addition, the electrical properties of ultra-thin films demonstrated an enhancement by employing a 50 nm-thick buffer layer of polycrystalline and stoichiometric $TiO_2$. In this case, conductive films were obtained down to a thickness of 5 nm. This result highlights the possibility to design devices with ultra-thin conductive films, which is a thickness difficult to achieve with metals.

Optical characterizations show that the Ta doping changes the optical response as a consequence of the increased charge carrier density. Indeed, the optical absorption in the UV range blue-shifts with the Ta content, according to the Moss-Burstein effect, while the absorption in the IR range increases because of free carriers.

The estimated optical band gaps increase with the Ta content for films 50-200 nm thick, while it starts to decrease for 20 nm films, down to a value typical of undoped $TiO_2$ for 10 nm-thick films.

Notably, both the electrical and the optical properties demonstrated no relevant changes in the thickness range from 200 nm down to 50 nm.

The effective mass of Ta:$TiO_2$ films was estimated as well, and the results are in accordance with theoretical calculations from the literature for a Ta-doped anatase phase. Moreover, the predicted increment of the effective mass with the Ta content is confirmed. Finally, the plasma energy was calculated to be in the near/mid-IR range, as expected for a TCO with a charge carrier density of the order of $10^{21}$ $cm^{-3}$.

The overall results, especially the fine tunability of the electrical and optical properties by means of the Ta content and the investigation of the thickness dependence of the film properties, show that Ta:$TiO_2$ films could be suitable as transparent conductive components in optoelectronic applications as well as for plasmonic applications in the IR range.

## Author Contributions

Beatrice R. Bricchi: writing – original draft, writing – review & editing, data curation, formal analysis, investigation and conceptualization.

Maria Sygletou and Giancarlo Terraneo: formal analysis, investigation and writing – review & editing.

Luca Ornago: formal analysis, investigation, conceptualization and writing – review & editing.

Cristina Mancarella, Lorenzo Stasi, Francesco Rusconi, Erika Mogni and Matteo Ghidelli: investigation and writing – review & editing.

Andrea Li Bassi, Francesco Bisio and Paolo Biagioni: supervision, conceptualization writing – review & editing.

## Conflicts of interest

There are no conflicts to declare.

## Acknowledgements

The authors thank Prof. M. Canepa and Dr. M. Magnozzi for useful discussion.

This project has received funding from the European Union's Horizon 2020 research and innovation programme under the Marie Skłodowska- Curie grant agreement no. 799126.

## References

1. S. C. Dixon, D. O. Scanlon, C. J. Carmalt, I.P. Parkin, *J. Mater. Chem. C,* 2016*,* **4**, 6946–6961.

2. D. H. Kim, S. Lee, J. H. Park, J. H. Noh, I. J. Park, W. M, Seong, K. S. Hong*, Sol. Energy Mater. Sol. Cells,* 2021, **96***,* 276–280.

3. S. Dias, S. Chirakkara, N. Patel, S. B. Krupanidhi, *J. Mater. Sci. Mater. Electron.,* 2018, **29***,* 2131–2139.

4. T. Hanada, T. Negishi, I. Shiroishi, T. Shiro, *Thin Solid Films,* 2010, **518***,* 3089–3092.

5. S. H. Park, J. B. Park, P. K. Song, *Curr. Appl. Phys.,* 2010, **10***,* S488–S490.

6. D. S. Ginley, J. D. Perkins *Handbook of Transparent Conductors*., Springer, Boston, MA, 2011.

7. F. Wang, M. Z. Wu, Y. Y. Wang, Y. M. Yu, X. M. Wu, L. J. Zhuge, *Vacuum,* 2013, **89**, 127–131.

8. G. Wan, S. Wang, X. Zhang, M. Huang, Y. Zhang, W. Duan L. Yi., *Appl. Surf. Sci.,* 2015, **357**, 622–625.

9. R. L. Moss, E. Tzimas, H. Kara, P. Willis, J. Kooroshy, *Assessing Rare Metals as Supply-Chain Bottlenecks in Low-Carbon Energy Technologies, JRC Scientific and Technical Reports, EUR 24884*, 2011.

10. H. Tang, K. Prasad, R. Sanjinès, P. E. Schmid, F. Lévy, *J. Appl. Phys.,* 1994, **75**, 2042–2047.

11. A. Fujishima, T. N. Rao, D. A. Tryk, *J. Photochem. Photobiol. C Photochem. Rev.,* 2000, **1**, 1–21.

12. T. Bak, J. Nowotny, M. Rekas, C. C. Sorrell, *Int. J. Hydrog. Energy,* 2002, **27**, 991–1022.

13. A. Hagfeldt, G. Boschloo, L. Sun, L. Kloo, H. Pettersson, *Chem. Rev.,* 2010, **110**, 6595–6663.

14. J. Osorio-Guillén, S. Lany, A. Zunger, *Phys. Rev. Lett.,* 2008, **100**, 036601.

15. P. Mazzolini, P. Gondoni, V. Russo, D. Chrastina, C. S. Casari, A. Li Bassi. *J. Phys. Chem. C,* 2015, **119**, 6988–6997.

16. H. Anh Huy, B. Aradi, T. Frauenheim, P. Deák, *J. Appl. Phys.,* 2012, **112**, 016103.

17. Y. Furubayashi, T. Hitosugi, Y. Yamamoto, K. Inaba, G. Kinoda, Y. Hirose, T. Shimada, T. Hasegawa. *Appl. Phys. Lett.,* 2005, **86**, 252101.

18. T. Hitosugi, Y. Furubayashi, A. Ueda, K. Itabashi, K. Inaba, Y. Hirose, G. Kinoda, Y. Yamamoto, T. Shimada, T. Hasegawa. *Jpn. J. Appl. Phys.,* 2005, **44**, L1063.

19. M. Neubert, S. Cornelius, J. Fiedler, T. Gebel, H. Liepack, A. Kolitsch, M. Vinnichenko, *J. Appl. Phys.,* 2013, **114**, 083707.

20. D. C. Qi, A. R. Barman, L. Debbichi, S. Dhar, I. Santoso, T. C. Asmara, H. Omer, K. Yang, P. Krüger, A. T. Wee, T. Venkatesan, *Phys. Rev. B,* 2013, **87**, 245201.

21. H. Kamisaka, T. Hitosugi, T. Suenaga, T. Hasegawa, K. Yamashita, *J. Chem. Phys.,* 2009, **131**, 034702.

22. S. A. Maier, *Curr. Nanosci.,* 2005, **1.1**, 17-22.

23. A. V. Kildishev, A. Boltasseva, V. M. Shalaev, *Science,* 2013, **339***,* 6125.

24. G. V. Naik, V. M. Shalaev, A. Boltasseva, *Adv. Mater.,* 2013, **25**, 3264–3294.

25. Z. Wang, C. Chen, K. Wu, H. Chong, H. Ye, *Phys. Status Solidi A,* 2019, **216**, 1700794.

26. A. V. Chichagov, Information-calculating system on crystal structure data of minerals (MINCRYST), *Materials Science Forum*, 193–198, 1994.

27. P. M. Oliver, G. W. Watson, E. T. Kelsey, S. C. Parker, *J. Mater. Chem.,* 1997, **7**, 563–568.

28. C. Yang, Y. Hirose, S. Nakao, T. Hasegawa, *J. Cryst. Growth,* 2013, **376***,* 66–69.

29. A. Li Bassi, D. Cattaneo, V. Russo, C. E. Bottani, *J. Appl. Phys.,* 2005, **98**, 074305.

30. U. Balachandran, N. G. Eror, *J. Solid State Chem.,* 1982, **42**, 276–282.

31. Y. Liu, Y. D. Qiao, G. Yang, *Appl. Phys. A,* 2018, **124**, 530.

32. P. Mazzolini, V. Russo, C. S. Casari, T. Hitosugi, S. Nakao, T. Hasegawa, A. Li Bassi, *J. Phys. Chem. C,* 2016*,* **120**, 18878–18886.

33. P. Deák, B. Aradi, T. Frauenheim, *Phys. Rev. B,* 2012, **86**, 195206.

 

34. B. Z. Dong, G. J. Fang, J. F. Wang, W. J. Guan, X. Z. Zhao, *J. Appl. Phys.* 2007, **101**, 033713.

35. D. C. Look, K. D. Leedy, A. Kiefer, B. Claflin, N. Itagaki, K. Matsushima, I. Suhariadi, *Opt. Eng.,* 2013, **52**, 033801.

36. D. C. Look, *Mater. Sci. Semicond. Process,* 2017*,* **69**, 2–8.

37. S. Agarwal, M. S. Haseman, K. D. Leedy, D. J. Winarski, P. Saadatkia, E. Doyle, L. Zhang, T. Dang, V. S. Vasilyev, F. A. Selim, *J. Electron. Mater.,* 2018, **47**, 2271–2276.

38. T. Okada, T. Kawashima, T. Mori, K. Washio, *Thin Solid Films,* 2020, **701**, 137954.

39. J. Nomoto, J. Oda, T. Miyata, T. Minami, *Thin Solid Films,* 2010, **519**, 1587–1593.

40. C. Lin, X. Li, C. Xu, *J. Mater. Sci. Mater. Electron.,* 2019, **30**, 721–730.

41. G. E. Jellison, L. A. Boatner, J. D. Budai, B. S. Jeong, D. P. Norton, *J. Appl. Phys.,* 2003, **93**, 9537–9541.

42. S.Tanemura, L. Miao, P. Jin, K. Kaneko, A. Terai, N. Nabatova-Gabain, *Appl. Surf. Sci.,* 2003, **212–213***,* 654–660.

43. N. Martin, C. Rousselot, D. Rondot, F. Palmino, R. Mercier, *Thin Solid Films,* 1997, **300**, 113–121.

44. L. Sun, P. Hou, *Thin Solid Films,* 2004, ***455–456,*** 525–529.

45. A.V. Manole, M. Dobromir, M. Gîrtan, R. Mallet, G. Rusu, D. Luca, *Ceram. Int.,* 2013, **39**, 4771–4776.

46. Y. R. Park, K. J. Kim, *Thin Solid Films,* 2005, **484**, 34–38.

47. E. Burstein, *Phys. Rev.,* 1954, **93**, 632–633.

48. W. Zhao, L. He, X. Feng, C. Luan, J. Ma, *CrystEngComm,* 2018, **20**, 5395–5401.

49. H. Poelman, H. Tomaszewski, D. Poelman, D. Depla, R. D. Gryse, *Surf. Interface Anal.,* 2004, **36**, 1167–1170.

50. A. Brudnik, H. Czternastek, K. Zakrzewska, M. Jachimowski, *Thin Solid Films,* 1991, **199**, 45–58.

51. A. Agrawal, R. W. Johns, D. J. Milliron, *Annu. Rev. Mater. Res.,* 2017, **47**, 1–31.

52. B. B. Varga, *Phys. Rev.,* 1965, **137**, 1896–1902.

53. A. Mooradian, G. B. Wright, *Phys. Rev. Lett.,* 1966, **16**, 999–1001.

54. M. Schubert, *Infrared Ellipsometry on Semiconductor Layer Structures: Phonons, Plasmons, and Polaritons*, Springer Science & Business Media, 2004.

55. M. Bass, E. W. Van Stryland, D. R. Williams, W. L. Wolfe, *Handbook of Optics: Fundamentals, techniques, and design*, McGraw-Hill, 1995.

56. H. A. Huy, B. Aradi, T. Frauenheim, P. Deák, *Phys. Rev. B,* 2011, **83**, 155201.

57. Y. Hirose, N. Yamada, S. Nakao, T. Hitosugi, T. Shimada, T. Hasegawa, *Phys. Rev. B,* 2009, **79**, 165108.

58. T. J. Coutts, D. L. Young, X. Li, *MRS Bull.* **2000**, *25*, 58–65.

59. A. Abdolahzadeh Ziabari, S. M. Rozati, *Phys. B Condens. Matter* **2012**, *407*, 4512–4517.

60. A. Jain, P. Sagar, R. M. Mehra, *Solid-State Electron.* **2006**, *50,* 1420–1424.

61. B. E. Sernelius, K. F. Berggren, Z. C. Jin, I. Hamberg, C. G. Granqvist, *Phys. Rev. B* **1988**, *37*, 10244–10248.

62. R. J. Gonzalez, R. Zallen, H. Berger, *Phys. Rev. B* **1997**, *55*, 7014–7017.

63. M. Eldlio, F. Che, M. Cada, *IAENG Transactions on Engineering Technologies,* 2014*,* 41–49.

64. P. Mazzolini, T. Acartürk, D. Chrastina, U. Starke, C. S. Casari, G. Gregori, A. Li Bassi, *Adv. Electron. Mater.,* 2016, **2**, 1500316.

65. G. S. Pawley, *J. Appl. Crystallogr.* 1981, **14**, 357–361.

66. C. Toccafondi, S. Uttiya, O. Cavalleri, G. Gemme, E. Barborini, F. Bisio, M. Canepa, *Journal of Physics D: Applied Physics,* 2014, **47.48**, 485301.

67. B. Johs, C. M. Herzinger, J. H. Dinan, A. Cornfeld, J. D. Benson, *Thin Solid Films,* 1998, ***313–314***, 137–142.

68. M. Magnozzi, S. Terreni, L. Anghinolfi, S. Uttiya, M. M. Carnasciali, G. Gemme, M. Neri, M. Principe, I. Pinto, L.-C. Kuo, S. Chao, M. Canepa, *Optical Materials,* 2018, **75**, 94-101.

## Table of contents

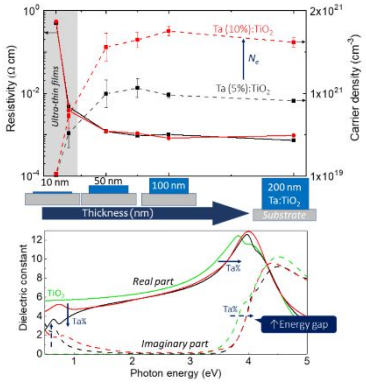


The evolution of optical and electronic properties of Ta-doped TiO2 films is investigated as thickness is decreased down to 5 nm and as a function of Ta doping (5-10% at.). The correlation between the observed behavior and structural properties is discussed, showing a high degree of tunability.

**Optical and electronic properties of transparent conducting Ta:$TiO_2$ thin and ultra-thin films: effect of doping and thickness**

*Beatrice R. Bricchi*, Maria Sygletou, Luca Ornago, Giancarlo Terraneo, Francesco Bisio, Cristina Mancarella, Lorenzo Stasi, Francesco Rusconi, Erika Mogni, Matteo Ghidelli, Paolo Biagioni, Andrea Li Bassi*

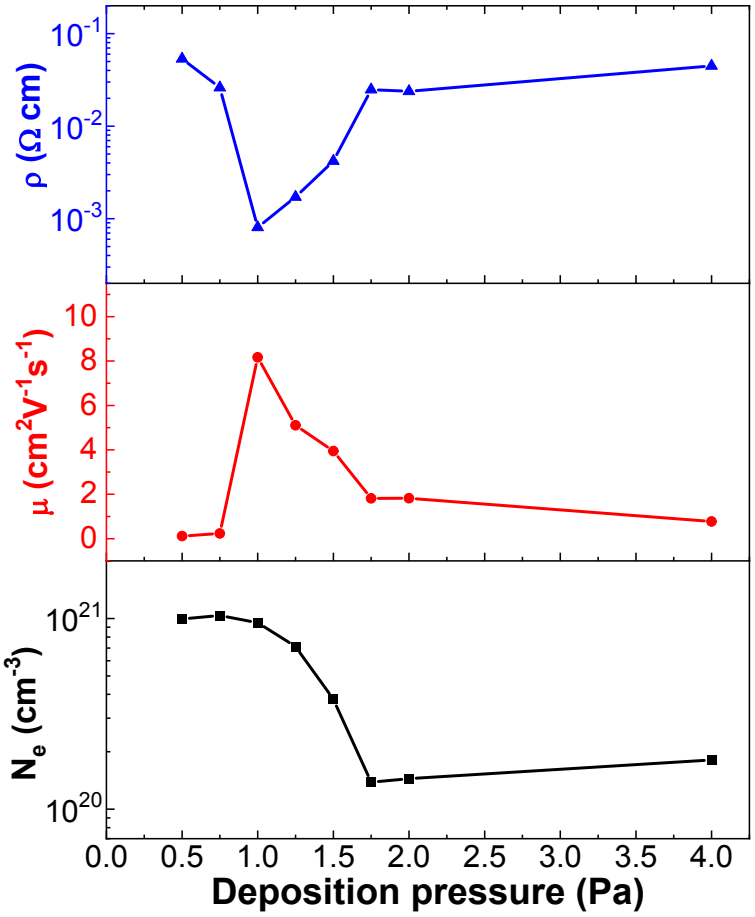


Figure S1 - Resistivity ($\rho$), charge carrier density ($N_e$) and mobility ($\mu$) as a function of background oxygen pressure ($P$) during deposition of Ta(5%):$TiO_2$ films thick 200 nm.

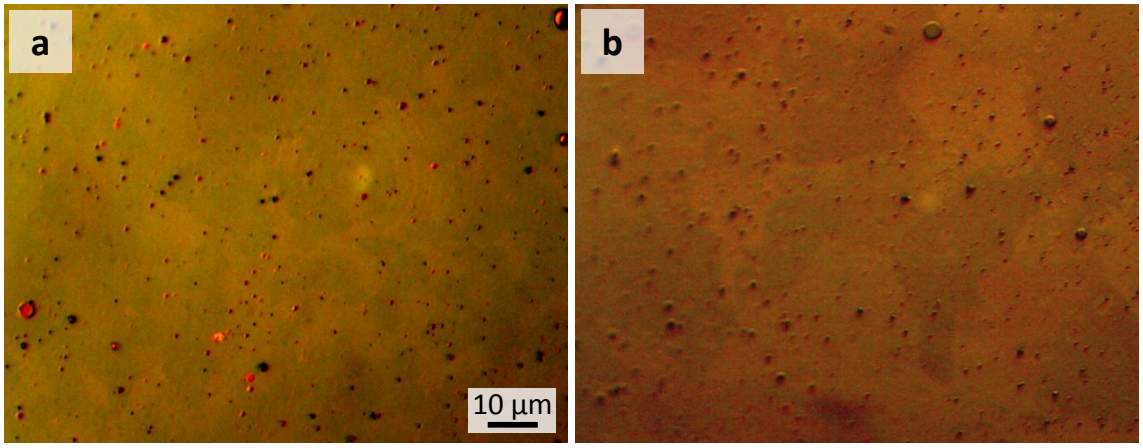


Figure S2 - Optical microscope images of surfaces of 200 nm-thick vacuum-annealed (a) Ta(5%):$TiO_2$ and (b) Ta(10%):$TiO_2$. All samples were deposited on glass substrate.

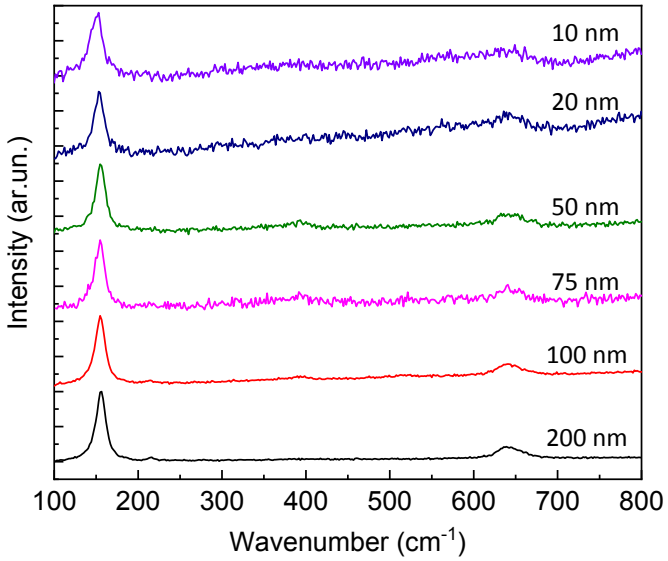


Figure S3 - Raman spectra of Ta(10%):$TiO_2$ films at different thickness, i.e. from 10 up to 200 nm.

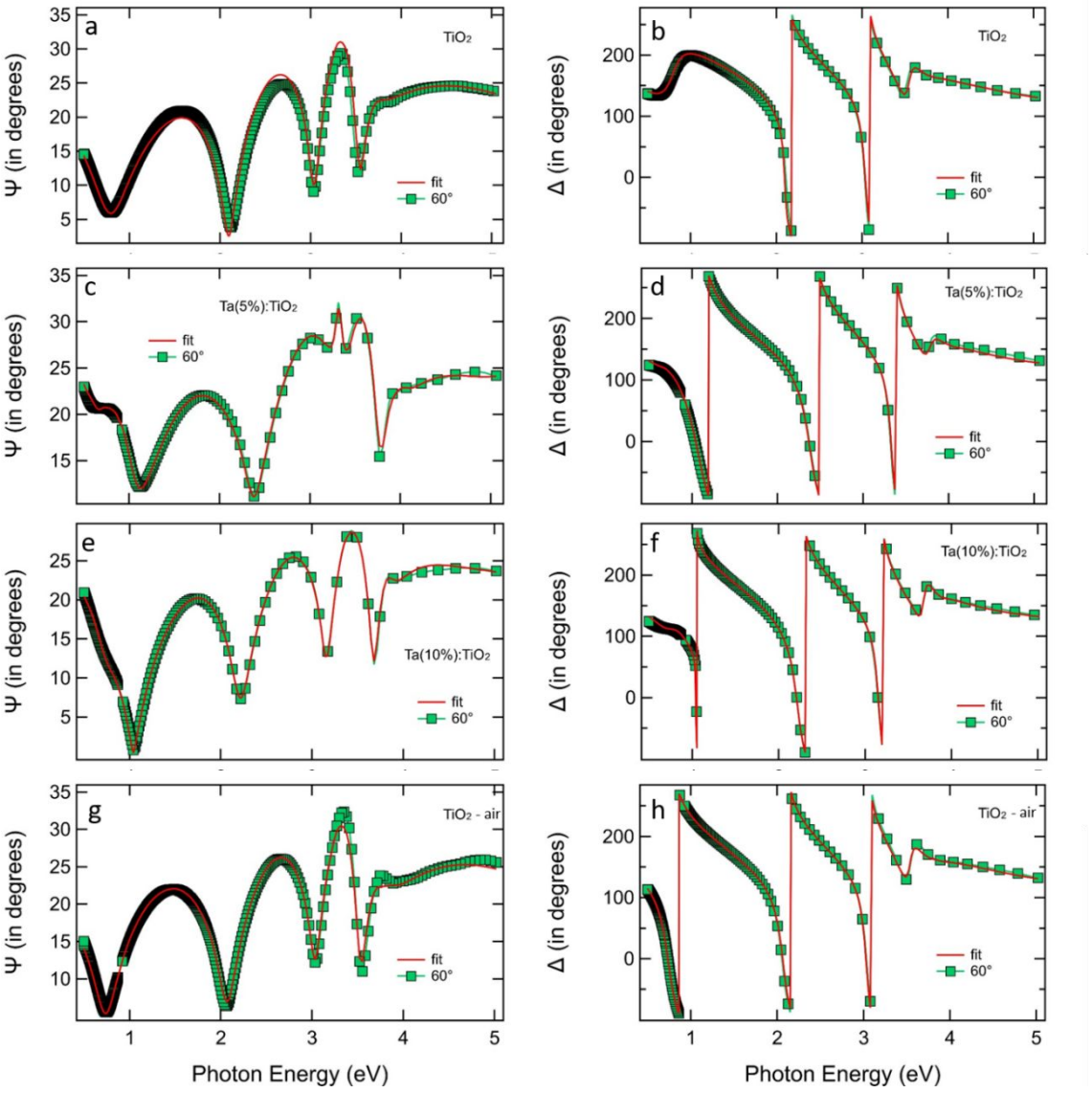


Figure S4 - Ellipsometric angles Ψ (left) and Δ (right) as a function of photon energy for (a, b) vacuum-annealed $TiO_2$, (c, d) Ta(5%):$TiO_2$, (e, f) Ta(10%):$TiO_2$ and (g, h) air-annealed $TiO_2$ films thick 200 nm and grown on Si substrates, acquired with incident angle of 60°. Squares and lines represent experimental data and theoretical fit, respectively.

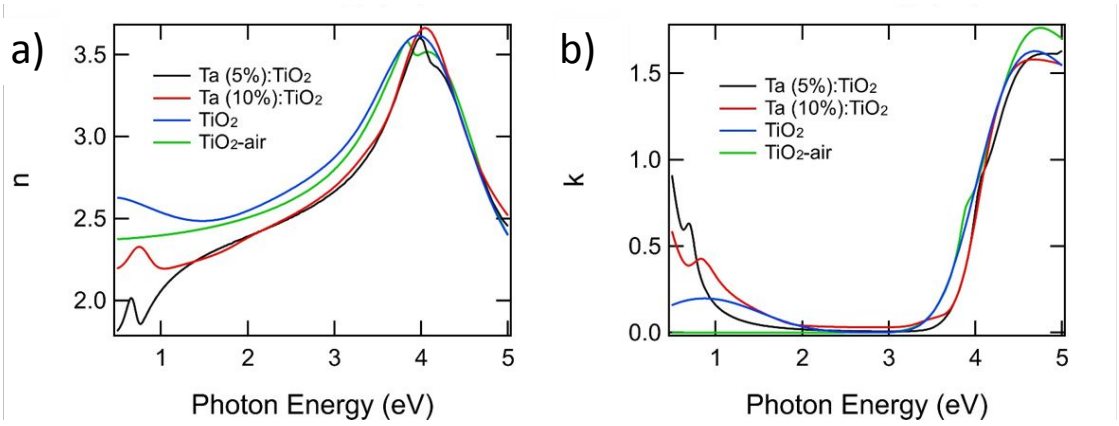

Figure S5 - (a) Refractive index (n) and (b) extinction coefficient (k) of the Ta:$TiO_2$ films as extracted from the dielectric function. Measurements on vacuum- and air-annealed $TiO_2$ films are reported for reference.

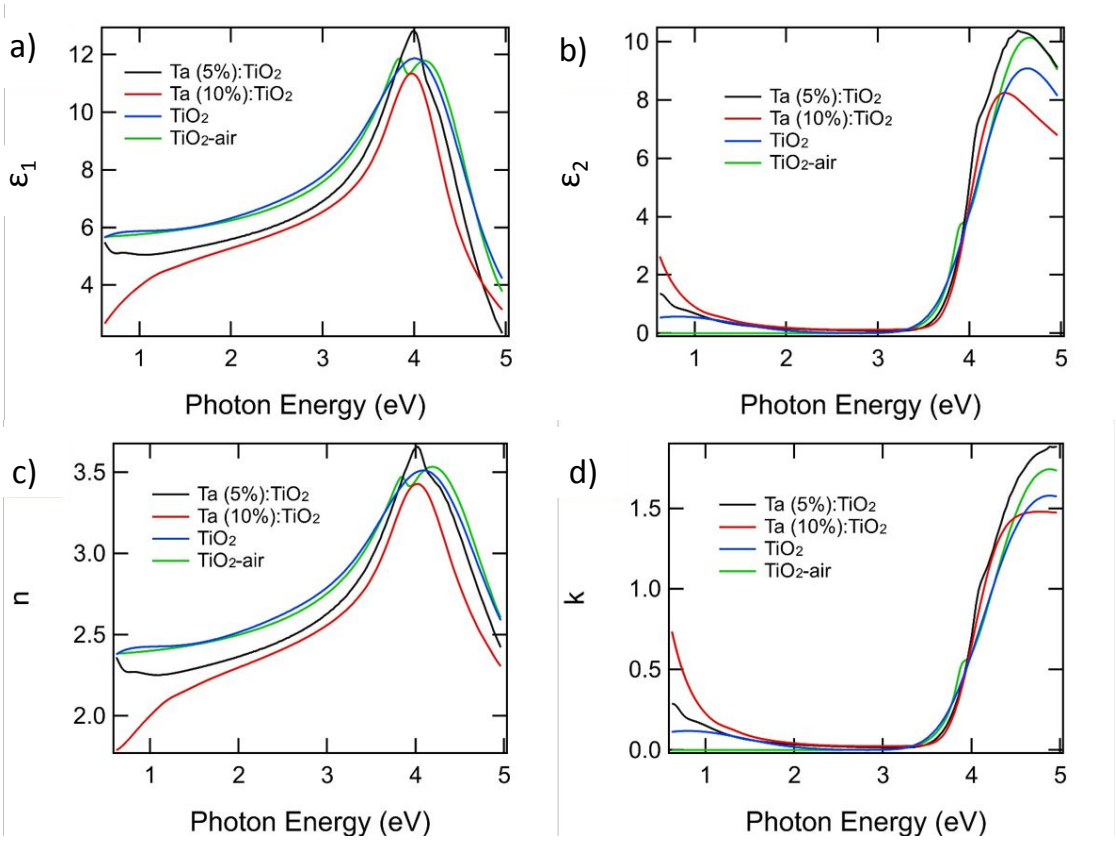


Figure S6 - (a) Real and (b) imaginary parts of the dielectric constant of Ta:$TiO_2$ films of different doping levels (5,10% at.), grown on soda-lime substrates, as extracted from the modelling of their transmission measurements by applying in the model the optical constants of Fig. 5. (c) Refractive index n and (d) extinction coefficient k of the Ta:$TiO_2$ films as extracted from the dielectric function. Measurements on vacuum- and air-annealed $TiO_2$ films (blue and green lines respectively) are reported for reference.

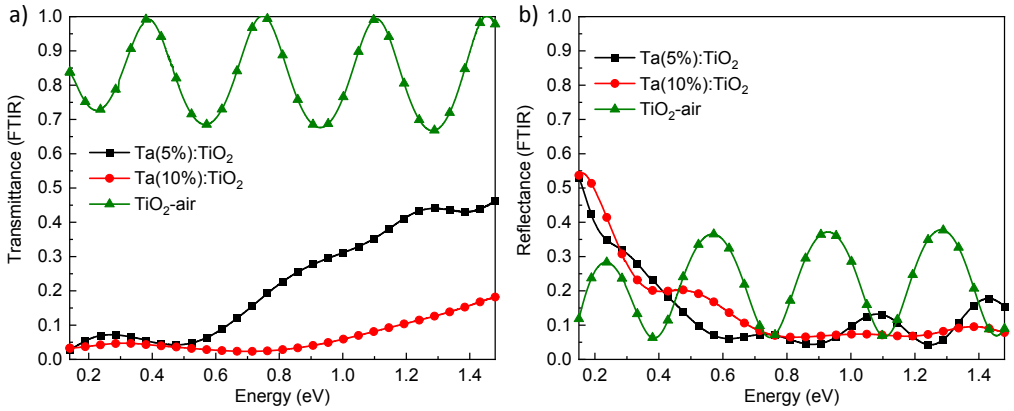


Figure S7 - (a) Transmittance and (b) reflectance spectra collected by Fourier Transform Infrared Spectroscopy (FTIR) of Ta(5%):$TiO_2$, Ta(10%):$TiO_2$ and air-annealed $TiO_2$ ($TiO_2$-air) films thick 670 nm and grown on $CaF_2$ substrate.